

Article

Design and Optimization of Potentially Low-Cost and Efficient MXene/InP Schottky Barrier Solar Cells via Numerical Modeling

Mohammad Saleh N Alnassar 

Department of Electrical Engineering, College of Engineering, Qassim University, Buraydah 51452, Saudi Arabia; msnsaar@qu.edu.sa

Abstract: This paper uses numerical modeling to describe the design and comprehensive analysis of cost-effective MXene/n-InP Schottky barrier solar cells. The proposed design utilizes $Ti_3C_2T_x$ thin film, a 2D solution-processible MXene material, as a Schottky transparent conductive electrode (TCE). The simulation results suggest that these devices can achieve power conversion efficiencies (PCEs) exceeding 20% in metal–semiconductor (MS) and metal–interlayer–semiconductor (MIS) structures. Combining the proposed structures with low-cost InP growth methods can reduce the gap between InP and other terrestrial market technologies. This is useful for specific applications that require lightweight and radiation-hard solar photovoltaics.

Keywords: solar cells; modeling; simulation; Schottky junction; InP; MXene; photovoltaic efficiency; optimization

1. Introduction

Renewable energy sources, such as biomass, geothermal, wind, and solar are available for sustainable use if effectively managed. Among these sources, solar energy stands out as the most promising and rapidly expanding alternative for commercial and domestic power needs [1]. The renewable energy industry has witnessed remarkable growth due to technological advancements in materials science and solar photovoltaic cell processing techniques. The absorber (or base layer), which is responsible for light absorption, is a key factor in the high efficiency of solar cells [2].

Due to its direct bandgap of ~ 1.34 eV, which is well-matched to the solar spectrum, indium phosphide (InP) is a promising absorber material for high-efficiency solar photovoltaic cells. This is in addition to its superior radiation hardness [3], as well as its absorption coefficient, which is considerably larger than that of its close competitor (GaAs) over the energy range of 1.30–2.7 eV [4], making it particularly attractive for settings with high radiation levels, such as space, nuclear, and high-altitude environments. Despite these desirable features, InP is still not competitive in the terrestrial solar cell market [5]. Some of the reasons why this is the case are the high processing costs and the epitaxial growth requirements [5,6]. The champion InP solar cell is a metal organic chemical vapor deposited (MOCVD) $n^+/p/p^+$ homojunction structure that requires multiple doping-controlled epitaxial growth steps in addition to growing lattice-matched passivation window layers, both of which are examples of costly materials and processing [7]. The power conversion efficiency (PCE) of the InP champion cell, at $\sim 24.2\%$, lags behind that of the GaAs cell, which is $\sim 29.1\%$ [8], and falls short of the Shockley–Queisser limit of $\sim 33.7\%$ for homojunction InP [9]. These figures suggest that there is room for improving these cells' efficiency.

Research efforts to reduce the cost of InP solar cells have been ongoing since the late 1970s. Over the years, researchers have explored alternative structures to the costly p^+/n or n^+/p InP homojunction. These alternatives include n-ITO/p-InP [10–13], n-CdS/p-InP [14–16], and other heterojunctions that utilize carrier selective contacts such as TiO_2 [17] and ZnO [18,19]. Additionally, InP-based Schottky junctions that consist of



Citation: Alnassar, M.S.N. Design and Optimization of Potentially Low-Cost and Efficient MXene/InP Schottky Barrier Solar Cells via Numerical Modeling. *Condens. Matter* **2024**, *9*, 17. <https://doi.org/10.3390/condmat9010017>

Academic Editors: Viorel-Puiu Paun, Eugen Radu, Maricel Agop and Mircea Olteanu

Received: 16 January 2024
Revised: 22 February 2024
Accepted: 29 February 2024
Published: 3 March 2024



Copyright: © 2024 by the author. Licensee MDPI, Basel, Switzerland. This article is an open access article distributed under the terms and conditions of the Creative Commons Attribution (CC BY) license (<https://creativecommons.org/licenses/by/4.0/>).

metal–semiconductor (MS) and metal–intermediate layer–semiconductor (MIS) structures have also been investigated [20–22]. In these early experimental investigations, conventional metals such as Au or Pt (on n-type InP) and Al or Sb (on p-type InP) were used to fabricate MS and MIS Schottky barrier solar cells and reported PCEs of $\leq 7\%$ measured under different conditions (AM 2 and AM 0). The intermediate layer commonly used in these studies is an ultrathin insulating material (InP anodic oxide) grown by anodizing the prepared surface of the InP substrate. Nowadays, intermediate layers beyond insulating oxides, known as Hole Transport-Electron Blocking Layer (HT-EBL) materials for n-type semiconductors and Electron Transport-Hole Blocking Layer (ET-HBL) materials for p-type semiconductors are investigated for use in MIS solar cells [23]. The InP solar cell has achieved PCEs of $\sim 19.3\%$ with fewer fabrication steps [5,17], thanks to combined research efforts for cost reduction. One of the most significant advancements is eliminating the need for MOCVD and epitaxial growth techniques [5].

Schottky barrier solar cells are the simplest to fabricate, requiring low thermal budgets, making them ideal for exploring novel materials and designs [24] and potentially low-cost for terrestrial applications. Such cells are commonly fabricated by depositing a thin metal layer with a high work function onto the top surface of an n-type semiconductor substrate with moderate doping [25]. As with any semiconductor device, low-resistance ohmic contacts are required and, therefore, formed on the back surface of the substrate (absorber layer) in these cells by depositing metal layers having work functions lower than that of an n-type semiconductor [26]. However, the front metal (semimetal) layer must be chemically and mechanically stable, optically transparent, and exhibit low resistance for efficient Schottky solar cells [27]. Finding a Schottky contact material for InP that satisfies these conflicting requirements is challenging; hence, fabricating efficient InP-based Schottky barrier solar cells remains elusive.

Two-dimensional materials, such as graphene and TMDs, are highly conductive and optically transparent and have lately been used to design innovative optoelectronic devices, including solar cells [28,29]. Two-dimensional materials and semiconductors forming Schottky junctions are promising for low-cost solar cells. The 2D materials act as transparent conductive electrodes (TCEs) and active layers to effectively collect and separate photoexcited carriers from semiconductors in these cells. The use of a novel class of 2D materials, known as MXenes (transition metal carbides, nitrides, and carbonitrides) [30], in solar photovoltaics has piqued the interest of experts since the first study in 2018 [31] due to their favorable attributes, including metallic electrical conductivity, high carrier mobility, excellent transparency, and exceptional mechanical properties. Recent experimental evidence showed that a prominent member of the MXene family, named titanium carbide MXene ($\text{Ti}_3\text{C}_2\text{T}_x$), where T_x represents different surface functional groups, such as $-\text{F}$, $-\text{O}$, and $-\text{OH}$, forms a high-quality large Schottky-barrier-height junction with n-Si and n-GaAs, resulting in an initial (unoptimized) PCEs of 5% and 9.69% [32,33], respectively.

Motivated particularly by the promising results obtained from MXene/n-GaAs solar cells [33], this paper presents, for the first time, the numerical modeling and optoelectronic simulation results obtained from MXene/n-InP Schottky solar cells designed using PC1D version 5.9 simulation software [34]. Benefiting from the tunable work function and high transparency of solution-processible $\text{Ti}_3\text{C}_2\text{T}_x$ thin film, this study investigates the potential use of this material as a Schottky TCE in combination with InP, a notable absorber material. The performance of these types of solar cells is systematically assessed by examining the critical structure and material parameters that influence both basic MS and more efficient MIS structures. Simulation parameters and models are initially calibrated using experimental data from the literature to ensure accuracy. This study provides valuable insights into the potential of low-cost MXene/InP solar cells, guiding future research.

2. Numerical Modeling and Simulation Methodology

The drift-diffusion transport equations for semiconductors serve as the basis for modeling solar cell physics. Specifically, the following system of five equations is considered:

$$J_n = \mu_n n \nabla E_{Fn} \quad (1)$$

$$J_p = \mu_p p \nabla E_{Fp} \quad (2)$$

$$\frac{\partial n}{\partial t} = \frac{\nabla \cdot J_n}{q} + G_L - U_n \quad (3)$$

$$\frac{\partial p}{\partial t} = \frac{\nabla \cdot J_p}{q} + G_L - U_p \quad (4)$$

$$\Delta^2 \phi = \frac{-\rho}{\epsilon} \quad (5)$$

where q is the elementary charge. In this system, Equations (1) and (2) relate the electron and hole current densities (J_n and J_p) to the mobilities (μ_n and μ_p), densities (n and p), and quasi-Fermi levels (E_{Fn} and E_{Fp}) of electrons and holes. Equations (3) and (4), referred to as the continuity equations, explain how electrons and holes move into and out of a semiconductor device by accounting for their flow into and out of a given region in the device, as well as the creation and annihilation processes within it (known as generation and recombination processes) using the electron–hole pairs generation rate (G_L) and electron and hole recombination rates (U_n and U_p). These equations are used to monitor the distribution and changes in the concentration of charge carriers over time. The final equation in the system, Equation (5), is Poisson's equation, which relates the electrostatic potential ϕ to the charge density per unit volume ρ and dielectric constant ϵ of a given region within the simulated device. Using the finite element method, PC1D solves this nonlinear partial differential equation system in one dimension with the appropriate boundary conditions derived from the device's realistic operational conditions. This approach has proven robust and accurate for various devices [27,35–38], including InP-based solar cells [39–41]. The simulations presented here are based on Boltzmann charge carrier statistics, recommended when implementing the default bandgap narrowing model in the simulations:

$$n = N_C e^{\frac{-(E_C - E_{Fn})}{kT}} \quad (6)$$

$$p = N_V e^{\frac{-(E_{Fp} - E_V)}{kT}} \quad (7)$$

Here, N_C and N_V are the effective density of states in the conduction and valence bands, E_C is the conduction band lower edge, E_V is the valence band upper edge, k is Boltzmann's constant, and T is the temperature. The parameters in the default bandgap narrowing model (PC1D5.9 BGN) were carefully calibrated to closely match the empirical model by Bugajski et al. [42] for n-type InP, as depicted in Figure 1, which gives good agreement with values measured experimentally. The default parameters of the low-field doping and temperature-dependent mobility model in PC1D are also changed to agree with the updated, more accurate model for InP by Sotoodeh et al. [43]. Table 1 shows the new parameters. Radiative (band-to-band) and Auger recombination processes are accounted for by adjusting the relevant parameters, in addition to doping and temperature-dependent Shockley–Read–Hall (SRH) recombination within the cell's bulk and at its surfaces. According to R.K. Ahrenkiel in [44], the data on minority carrier lifetimes and surface recombination velocities (SRVs) in n-InP show significant variation. The lifetimes can range from as low as 0.01 μs to 3.5 μs , while the SRVs can range from 200 cm s^{-1} to $5 \times 10^3 \text{ cm s}^{-1}$. These large variations depend on the growth method, material surface quality, and the measurement method used.

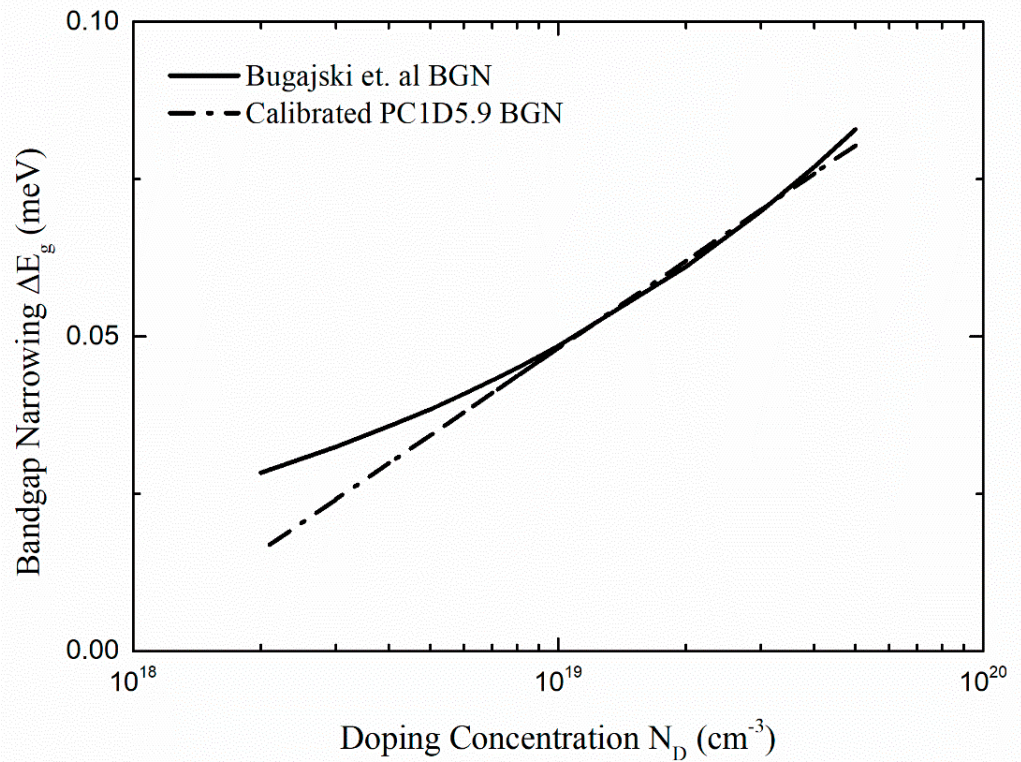


Figure 1. Comparison of bandgap narrowing results for different donor concentrations of n-type InP at 300 K [42].

Table 1. Modified mobility-fitting parameters in PC1D for InP simulations (300 K).

Parameter	μ_{\max} (cm ² /Vs)	μ_{\min} (cm ² /Vs)	N_{ref} (cm ⁻³)	α	β_1	β_2	β_3	β_4	v_{sat} (cm/s)
Electrons	5200	400	3×10^{17}	0.47	0	-2	3.25	0	2.6×10^7
Holes	170	10	4.87×10^{17}	0.47	0	-2	3	0	2.6×10^7

The schematic diagrams of MS and MIS structures designed in PC1D are shown in Figure 2. The two structures differ only by the presence of an ultrathin semi-insulating SI-InP layer. It can be realized using various methods, such as ion implantation of Fe, reaching resistivities $>10^7 \Omega\text{-cm}$, corresponding to a carrier concentration of $\sim 1.2 \times 10^8 \text{ cm}^{-3}$ [45]. If SI-InP retains desirable InP properties and is lattice-matched with the n-type absorber in the MIS structure, the MIS solar cells are expected to outperform the MS cells due to dark current reduction [20,21].

Schottky junctions are modeled in PC1D with a nonzero ‘surface barrier’ at the MS interface, causing band bending consistent with the semiconductor type. The ‘surface barrier’ value in this case is equivalent to the built-in potential barrier (qV_{bi}), as seen by the semiconductor electrons near the metal-to-n-semiconductor interface. Negative (positive) surface barrier values simulate upward (downward) band bending. The Schottky barrier height (Φ_b) is related to the built-in potential barrier qV_{bi} by the equation $\Phi_b = qV_{bi} + kT/q \ln(N_C/N_D)$, where N_D is the donor doping concentration of the semiconductor. The Schottky barrier height is also related to the metal’s ($\text{Ti}_3\text{C}_2\text{T}_x$ MXene) work function Φ_M by the equation $\Phi_b = \Phi_M - \chi_{\text{InP}}$, where χ_{InP} is the electron affinity of the semiconductor (n-InP), assuming a metal/n-InP semiconductor junction obeying the Schottky–Mott model [46].

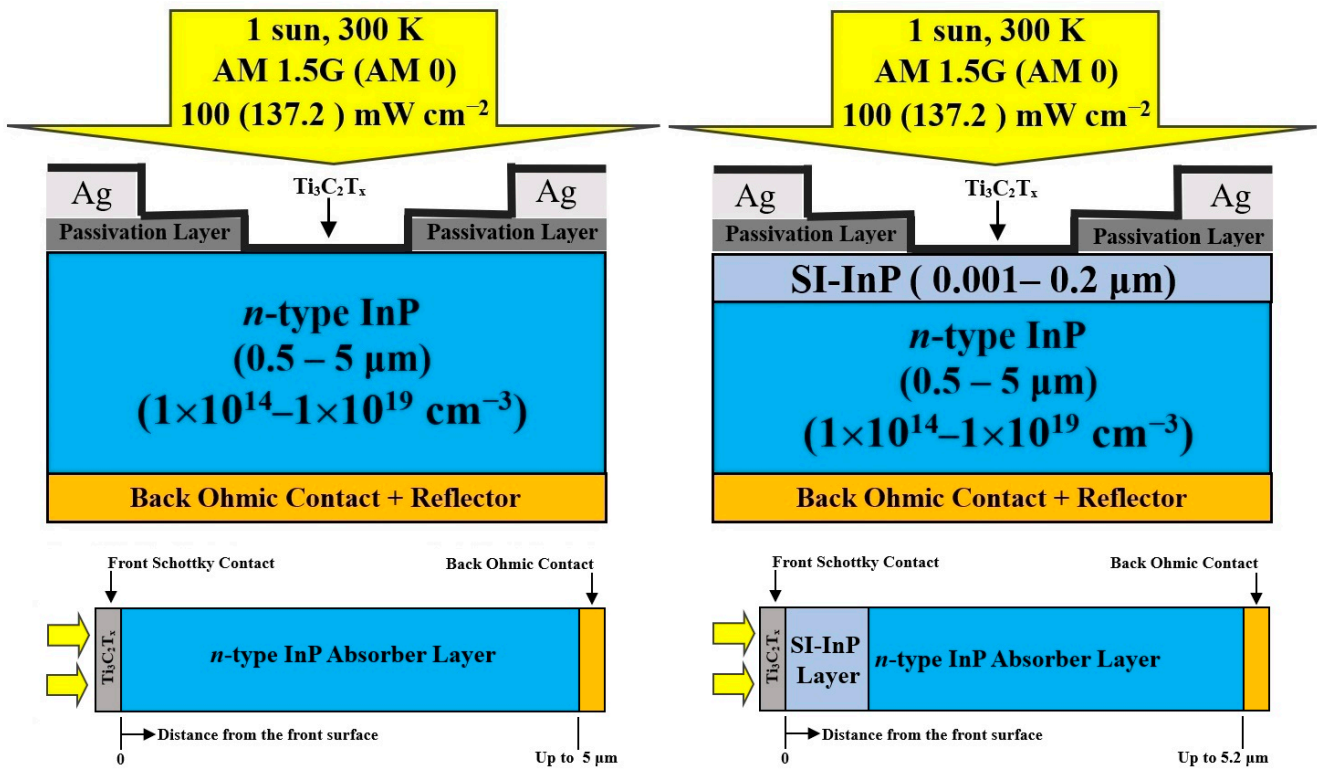


Figure 2. Schematic representations of MS and MIS MXene/ n -InP Schottky solar cells (top) and their equivalent 1D structures simulated in PC1D (bottom).

Modeling the MIS structure in PC1D is quite different from modeling the MS one, as including the intermediate layer gives rise to an additional potential barrier to the assumed ‘surface barrier’ value described above. The carrier concentration significantly drops when crossing from the n -InP region to the ultrathin SI-InP region, creating this additional potential barrier, given by $kT/q \ln(N_D/1.2 \times 10^8)$. Therefore, qV_{bi}^* can be defined as the overall built-in potential barrier, as seen by semiconductor electrons in the MIS structure due to both contributions. It is related to the ‘surface barrier’ value entered as a model parameter in PC1D by the equation $qV_{bi}^* = qV_{bi} + kT/q \ln(N_D/1.2 \times 10^8)$, accounting for the band bending observed across both regions. It is important to note that in the MIS structure, the metal is in direct contact with the SI-InP. Thus, $\Phi_b = qV_{bi} + kT/q \ln(N_C/1.2 \times 10^8)$.

A $\text{Ti}_3\text{C}_2\text{T}_x$ colloidal solution with a concentration of 0.01 mg mL^{-1} offered the optimum TCE thin film properties (work function of $\sim 5.5 \text{ eV}$, transmittance $\sim 90\%$, and series resistance of $\sim 10 \Omega$) [33]. Consequently, these values will serve as inputs in the initial simulation of the designed MXene/InP solar cell, which has an active area of 1 cm^2 . Table 2 lists the simulation parameters used in this work. The $\text{Ti}_3\text{C}_2\text{T}_x$ TCE thin film slightly improved the reflectance of GaAs upon introduction, and a reflectance of less than 16% was reported after the double-layer antireflection coating (DLARC) deposition of ZnS/MgF₂ [33]. The reflectance of InP is slightly less than that of GaAs (32.7% for InP and 35.9% for GaAs), as calculated by the OPAL 2 optical simulator [47] using refractive index data from Palik [48] and Aspenes et al. [49], respectively. Thus, this study assumes an average conservative reflectance value of 15% for the initial simulations. For completeness, the proposed solar cells were simulated under terrestrial AM 1.5G and space AM 0 spectra to assess if they yield dissimilar optimization outcomes.

Table 2. Parameters used for the initial simulation of MS and MIS MXene/n-InP solar cells.

Device Parameters		
Parameter	Value	Reference
Front surface barrier (qV_{bi}) [†]	0.956 eV *	Ti ₃ C ₂ T _x TCE thin film [33]
Exterior front reflectance	15% **	According to [33]
Front contact resistance	10 Ω **	Ti ₃ C ₂ T _x TCE thin film [33]
Back contact resistance	0.1 Ω	Assuming good ohmics [50]
Region Parameters (n-InP)		
Parameter	Value	Reference
Bandgap	1.344 eV	According to [51]
Electron affinity	4.38 eV	According to [51]
Thickness	3 μm *	Initial simulation
Mobility	Variable	According to [43]
Dielectric constant	12.61	According to [51]
Refractive index	Variable	(using inp.inr file)
Absorption coefficient	Variable	(using inp300.abs file)
Intrinsic concentration (300 K)	$1.3 \times 10^7 \text{ cm}^{-3}$	According to [51]
Doping concentration (N_D)	$1 \times 10^{15} \text{ cm}^{-3}$ *	Initial simulation
Bulk recombination lifetimes	1 μs	According to [44]
Front SRVs (S_n and S_p)	1000 cm s ⁻¹ **	According to [44]
Back SRVs (S_n and S_p)	1000 cm s ⁻¹	According to [44]
Region Parameters (SI-InP)		
Parameter	Value	Reference
Thickness	0.001 μm *	Initial simulation
Resistivity	10 MΩ·cm	Semi-insulating layer [45]
Front SRVs (S_n and S_p)	1000 cm s ⁻¹ **	According to [44]
Excitation Parameters		
Parameter	Value	
Spectrum	AM 1.5G and AM 0	
Constant intensity	100 mW cm ⁻² and 137.2 mW cm ⁻²	
Temperature	300 K	

[†] The parameter value must be a negative number in PC1D to invoke upward band bending. * These parameters are varied, while others are kept constant to find the optimum MS (MIS) structures. ** After optimization, these parameters are modified to explore possible performance gains.

3. Results and Discussions

To confirm the formation of a Schottky junction between the n-InP absorber layer and the Ti₃C₂T_x TCE, initial simulations were conducted under equilibrium conditions for the solar cell structures depicted in Figure 2, using the parameters listed in Table 2. The simulation results were used to assess the energy band diagrams and junction electrostatics. For the MS structure, an assumption was made that $\Phi_m = 5.50$ eV and $N_D = 1 \times 10^{15} \text{ cm}^{-3}$. Based on this, the value of qV_{bi} was determined to be ~0.956 eV, which was used as the front surface barrier value in the initial simulation (Table 2). The simulation shows that a Schottky barrier height Φ_b of ~1.12 eV is formed, as illustrated by the energy band diagram for the MS structure in Figure 3a. It should be noted that this figure depicts the region of

the n-InP layer where band bending takes place, which is within the first two micrometers from the MS junction.

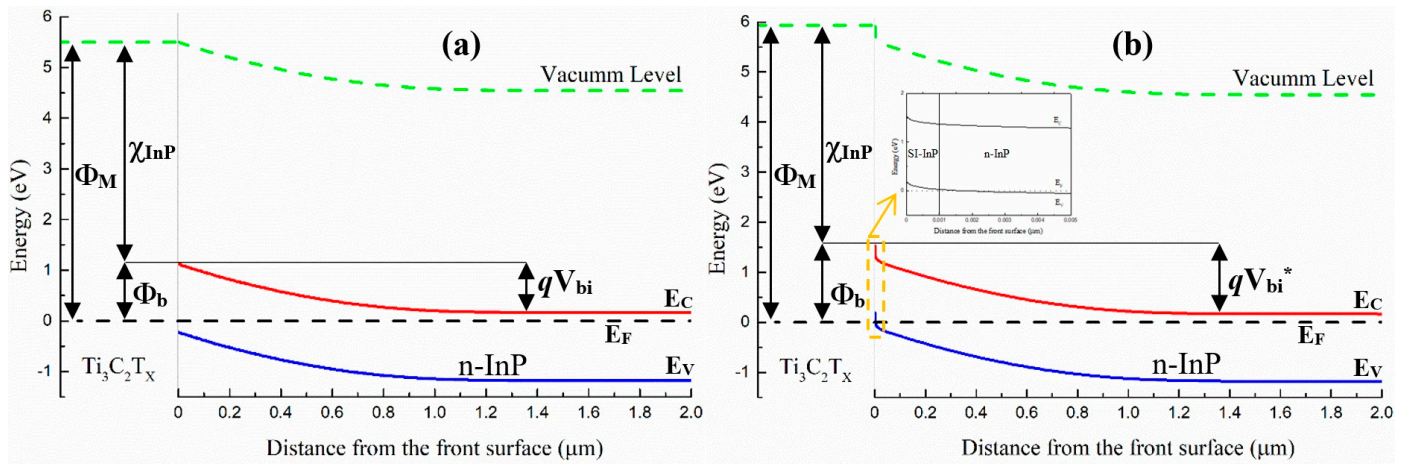


Figure 3. Simulation results showing the energy band diagram at equilibrium for the (a) MS and (b) MIS structures (only up to 2 μm is shown for both structures). The inset in (b) shows the effect of the 1 nm SI-InP interlayer on the energy levels within 5 nm from the MI junction in the MIS structure.

Figure 3b shows the effect of adding the 1 nm thick SI-InP layer (the MIS structure) on the energy band diagram, with an inset displaying the events occurring in the first five nanometers from the MI junction. As expected, based on the MIS discussion in Section 2, the resulting overall built-in potential barrier qV_{bi}^* of ~1.368 eV is composed of the front surface barrier used in simulating the MS structure (0.956 eV) and an additional potential barrier (~0.412 eV) due to the introduction of the SI-InP intermediate layer to the device. Consequently, in the case of the MIS structure, the simulated Schottky barrier height is ~1.53 eV, which is higher than that in the MS structure (~1.12 eV), in agreement with frequently reported observations in the aforementioned experimental studies on MS and MIS solar cells [20,22]. As can be clearly seen in Figure 3b and determined by the equation $\Phi_M = \Phi_b + \chi_{InP}$, the simulated Φ_b , in this case, corresponds to a higher metal work function Φ_M of ~5.91 eV, as opposed to the initially assumed value of 5.50 eV for the MS structure. The inset in Figure 3b indicates that even though the SI-InP layer is assumed to be n-type, with carrier concentrations approaching intrinsic values, the transition from the n-InP layer to the SI-InP layer causes the equilibrium Fermi level (E_F) to be positioned below the valence band upper edge (E_V) near the junction. This is unlike the situation in the MS structure, where E_F is above E_V . The electric field values near the MIS junction can reach as high as ~11 MV/cm, which is much higher than the ~17 kV/cm observed in the MS structure, positively aiding in the separation and transport of the photoexcited charge carriers within the device, as will be confirmed in later performance simulations.

3.1. Optimization of MS and MIS Structures

The $Ti_3C_2T_x$ work function can be tuned theoretically from ~1.6 eV to ~6.7 eV [52]. However, Si-based and GaAs-based Schottky solar cell experiments have shown work functions ranging from ~5 eV to ~5.5 eV [32,33]. Hence, this range, which corresponds to an expected built-in potential barrier (qV_{bi}) range from ~0.40 eV to ~1.20 eV ($N_D = 1 \times 10^{14} - 1 \times 10^{19} \text{ cm}^{-3}$), was considered for optimizing the MS cell. For the MIS cell, the same range is used; nonetheless, this range does not necessarily correspond to the same metal work function range as in the MS structure since the metal in the MIS structure comes into intimate contact with the highly resistive SI-InP interlayer, as opposed to the n-InP layer, with a much lower, nonvarying carrier concentration (~ $1.2 \times 10^8 \text{ cm}^{-3}$). The optimization

for both cells also involved varying the n-InP layer doping concentration (N_D) from 1×10^{14} to $1 \times 10^{19} \text{ cm}^{-3}$ and the n-InP layer thickness from 0.5 to 5 μm while keeping the remaining parameters fixed, as specified in Table 2. The SI-InP layer's thickness was varied from 0.001 to 0.2 μm for the MIS solar cell structure. Table 3 presents the optimized parameters for both structures, assuming a 300 K ambient temperature under the AM 1.5G and AM 0 spectra.

Table 3. Optimum parameter values for MXene/n-InP MS and MIS Schottky solar cells.

PC1D Design Parameter	Schottky Barrier Solar Cell Structure			
	MS		MIS	
	AM 1.5G	AM 0	AM 1.5G	AM 0
Front surface barrier qV_{bi} (eV)	1.015	1.075	0.865	0.865
Thickness of n-InP (μm)	5	2.5	1	1
Doping conc. of n-InP (cm^{-3})	1×10^{16}	1×10^{17}	1×10^{18}	1×10^{18}
Thickness of SI-InP (μm)	-	-	0.15	0.1

For the MS solar cell simulated under both solar spectra, the optimal combination of qV_{bi} and N_D in Table 3 corresponds to the imposed upper limit of $\text{Ti}_3\text{C}_2\text{T}_x$'s work function of ~ 5.5 eV, as expected. However, when the MS solar cell is simulated under the AM 0 solar spectrum, it requires half the thickness and a higher doping concentration to achieve the highest PCE compared to the one simulated under the AM 1.5G solar spectrum. The optimum base doping concentration value of $1 \times 10^{17} \text{ cm}^{-3}$ aligns with a previous study on p+/n InP-based homojunctions designed for space applications [53]. These outcomes are encouraging, especially if this structure is, for instance, used for unmanned aerial vehicle UAV applications, where weight and high radiation are significant concerns. Using less material would also mean lower costs, and higher doping concentrations are beneficial for enhanced radiation hardness in InP [41].

The situation differs for the MIS solar cell, where the optimum values for qV_{bi} , N_D , and the n-InP layer thickness are identical under both solar spectra. The optimum qV_{bi} value of ~ 0.865 eV is way below the maximum (1.135 eV) for an N_D of $1 \times 10^{18} \text{ cm}^{-3}$. Surprisingly, the performance is hardly affected beyond this point, unlike the situation with the MS structure. Note that the ideal thickness for the MIS solar cell structure (1.15 μm) is significantly lower than the MS structure thickness (5 μm) by almost a factor of five under the AM 1.5G spectrum and is less than one-half of the MS structure thickness (2.5 μm) under AM 0. This implies that solar arrays based on MIS structures will have higher specific power (W/Kg), making them more attractive for weight-sensitive applications [54].

The J-V characteristics simulated under AM 1.5G and AM 0 solar spectra for MS and MIS Schottky structures, along with performance data, are shown in Figure 4. Both structures performed better under AM 1.5G compared to AM 0, which agrees with previous investigations on the performance of InP-based solar cells under both spectra [53,55]. The introduction of SI-InP enhanced the open circuit voltage (V_{OC}) under AM 1.5G; however, it has led to lower short circuit current densities (J_{sc}) in the MIS structure. Despite this, the MIS structure has a higher fill factor (FF) and PCE under both spectra than the MS structure.

3.2. Performance Sensitivity to Optimization Parameters

Since this work is primarily concerned with designing low-cost InP-based Schottky solar cells for terrestrial applications, the simulation results shown in Figure 5 assume only the AM 1.5G spectrum to illustrate the performance sensitivity of the optimized MS and MIS structures to changes in the optimized parameters listed in Table 3.

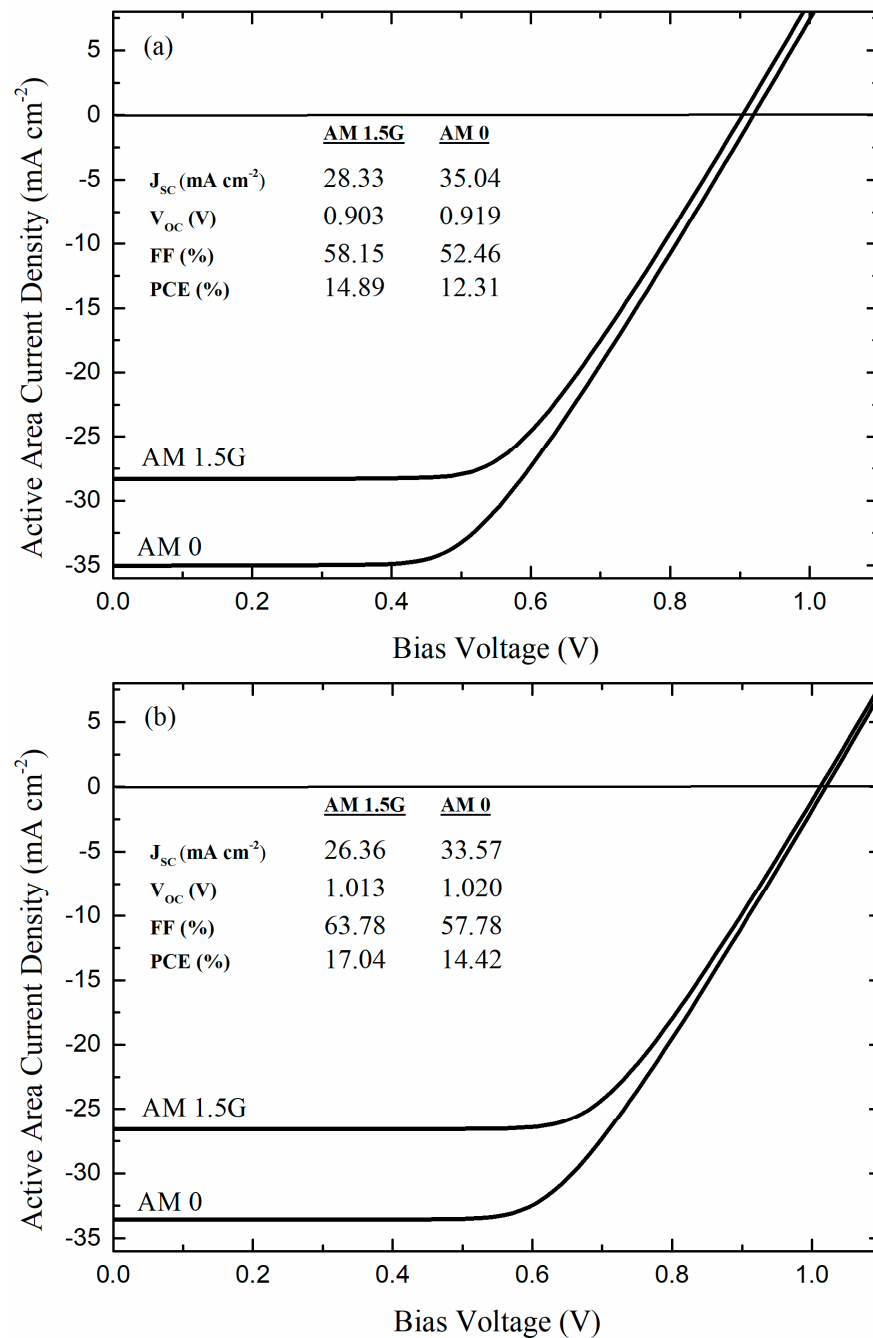


Figure 4. J-V characteristics and performance results for the optimum (a) MS and (b) MIS MXene/n-InP Schottky solar cells.

A specific threshold front surface barrier value exists for both structures, where the photovoltaic action diminishes due to the absence of (or very low) Φ_b for a given doping concentration. This corresponds to a metal with a work function comparable to or lower than an n-type semiconductor. According to the ideal MS junction's theory, this leads to the formation of an ohmic contact rather than a Schottky contact to the n-type semiconductor. The threshold qV_{bi} values are ~ 0.55 eV and ~ 0.1 eV for the MS and MIS structures. As displayed in Figure 5a, the performance of the MS structure is almost unchanged for $qV_{bi} < \sim 0.90$ eV, and afterward, the PCE and FF increase to their maximum values (14.89% and 58.15%), due to the improvement in V_{OC} . In the MIS structure, improvement in PCE and FF happens earlier, at qV_{bi} of ~ 0.45 eV. As of the influence of the n-InP absorber thickness (Figure 5b), the PCE of the MS structure noticeably increases at thicknesses

$< \sim 2 \mu\text{m}$ and keeps increasing very slightly afterward, but it starts to decrease beyond $15 \mu\text{m}$ (outside the range shown). For the MIS structure, the improvement in PCE due to J_{SC} occurs in the n-InP thickness range of $0.5\text{--}1 \mu\text{m}$, slightly decreases until $3 \mu\text{m}$, and then remains constant until $15 \mu\text{m}$, after which it decreases slightly (outside the range shown). Figure 5c depicts the influence of n-InP absorber doping concentration (N_{D}) on both structures, where J_{SC} starts to decrease at $N_{\text{D}} > 1 \times 10^{16} \text{cm}^{-3}$. However, this decrease is offset by a continuous increase in V_{OC} along the whole range of N_{D} in the MIS structure. The situation is different for the MS structure, since V_{OC} starts decreasing at $N_{\text{D}} > 1 \times 10^{16} \text{cm}^{-3}$, which causes the PCE to reach its maximum earlier than the MIS structure. Figure 6 shows the influence of SI-InP layer thickness on the MIS structure's performance. The increase in J_{SC} for thicknesses $> 0.01 \mu\text{m}$ is negated by the decrease in V_{OC} and the FF, leading to a delayed decrease in PCE after $0.1 \mu\text{m}$.

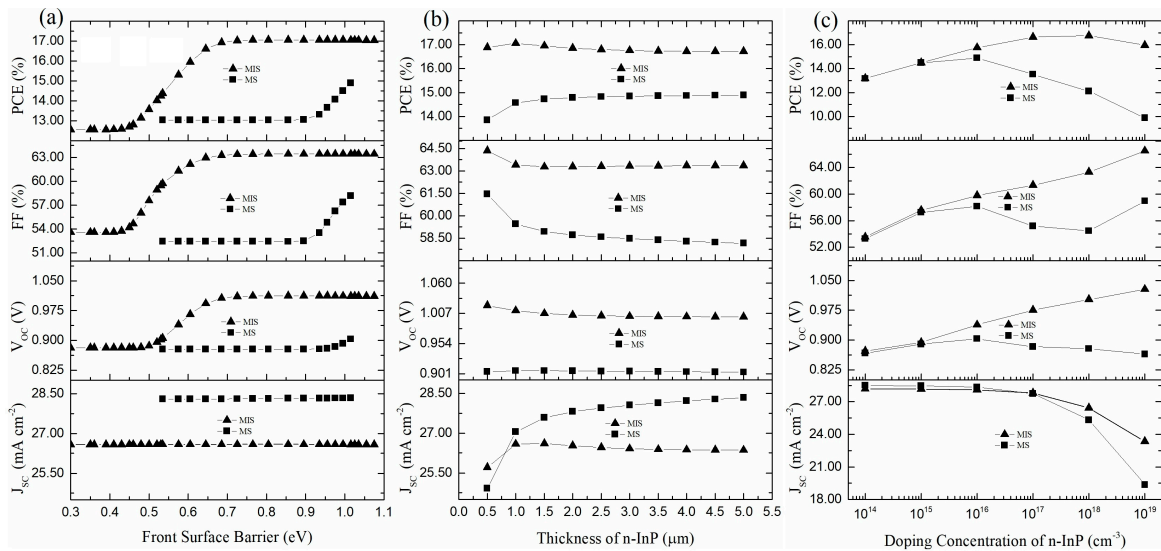


Figure 5. Performance sensitivity of MS and MIS MXene/n-InP Schottky solar cells to changes in (a) qV_{bi} , (b) n-InP layer thickness, and (c) its doping concentration.

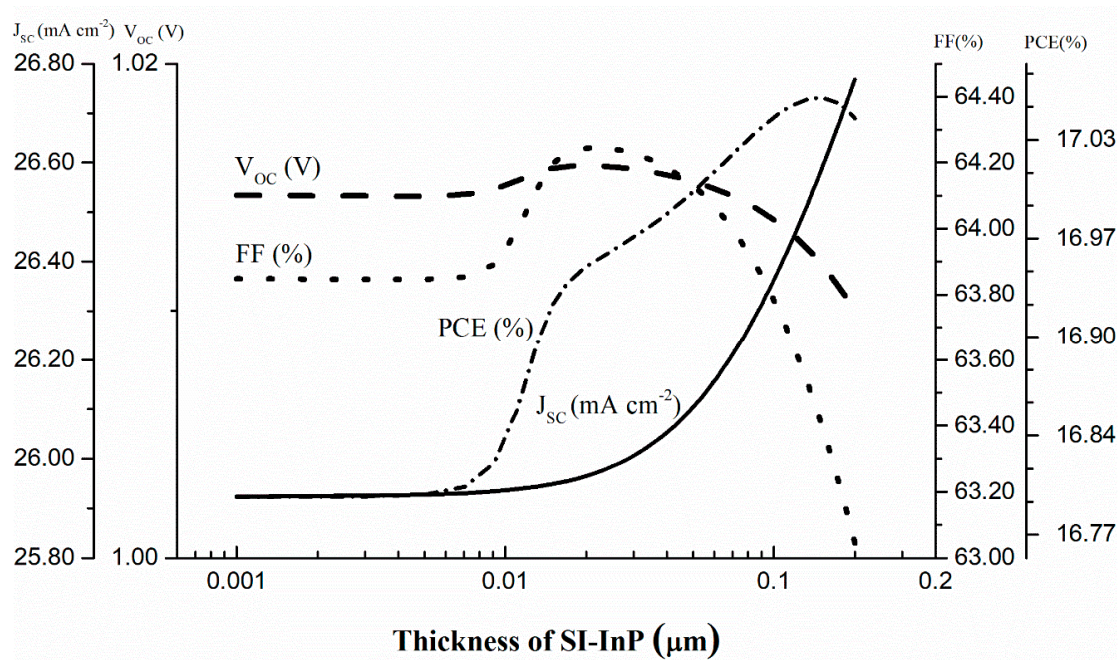


Figure 6. Effect of SI-InP thickness on the performance of MIS MXene/n-InP Schottky solar cell.

3.3. Possible Performance Gains

It is important to remember that the demonstrated results are based on various constraints, derived from reported measurements in pioneering experimental studies of Schottky solar cells with MXene TCEs [32,33]. These constraints include front contact series resistance of $10\ \Omega$, exterior front reflectance of 15%, and front SRV of $1 \times 10^3\ \text{cm s}^{-1}$. Additionally, all the simulations performed so far assume the absence of a back surface reflector.

The performance of both MS and MIS MXene/n-InP Schottky solar cells can be significantly improved if the above constraints can be relaxed. However, to be realistic, experimental evidence must justify such relaxation. The $10\ \Omega$ front contact series resistance is based on the reported series resistance for MXene/GaAs devices with the highest efficiency. It is assumed that the MXene thin film contacting the GaAs absorber is the device component contributing dominantly to this resistance. Regardless, the experimental measurements of both studies investigating MXene/Si and MXene/GaAs contacts showed consequential variability in terms of the measured sheet resistance of the deposited MXene thin film, which is a function of thickness, oxidation, chemical treatment/doping, and top metal grid mesh. This fact suggests that further experimentation with this novel material could decrease the series resistance, as observed in graphene and other 2D materials [28,56,57].

It has been demonstrated that traditional ARCs were experimentally optimized to produce an average reflectance of about 3.5% in InP-based solar cells, while novel optical management techniques have achieved values below this threshold [58,59]. Additionally, rear back surface reflectors reflecting over 90% of long wavelength photons ($\lambda > 900\ \text{nm}$) using double layer Ag/Cu contacts were demonstrated for GaInNAs solar cells, leading to enhanced photocurrent and, consequently, external quantum efficiency (EQE) [60].

The same argument of experimental variability is applied to the assumed value of SRV of $1 \times 10^3\ \text{cm s}^{-1}$ in the simulations. As discussed in Section 2, the value of SRV can be reduced to as low as $200\ \text{cm s}^{-1}$, depending on the InP growth method and surface quality/treatments [44].

Suppose both structures, as shown in Figure 2, incorporate an effective back surface reflector capable of reflecting 90% of non-absorbed solar radiation in the first pass; then, this can be simulated in PC1D by assuming a rear internal diffuse reflectance of 90% in the first and subsequent bounces. Figure 7 shows the results of the simulations, which reveal the projected enhancement in PCE for both MS and MIS structures as a result of improvement in the parameters above.

Based on the data presented in Figure 7, it is evident that the front contact series resistance and exterior front reflectance significantly impact the PCE of both cell structures. On the other hand, the front surface recombination velocities (SRVs) have a negligible effect on the PCE of the MIS structure, unlike the MS structure. However, the effect of this parameter is minor when compared to the impact of front contact series resistance and exterior front reflectance. The front contact's series resistance value could be improved experimentally, but $5\ \Omega$ was chosen as a realistic minimum value for now to avoid performance overestimation (Figure 7a), as mature solar cell technologies typically have area-normalized series resistance values that are much less than $5\ \Omega\text{cm}^2$ [61]. The J-V characteristics, simulated under the AM 1.5G solar spectrum for the MS and MIS structures after considering the improved potential gain parameters, are shown in Figure 8, along with performance data. Assuming a front contact series resistance of $5\ \text{ohms}$, a front surface reflectance of 5%, and front SRVs of $200\ \text{cm s}^{-1}$, these favorable figures are achieved by using the optimum parameter values, as listed in Table 3. All other parameters are fixed, as specified in Table 2.

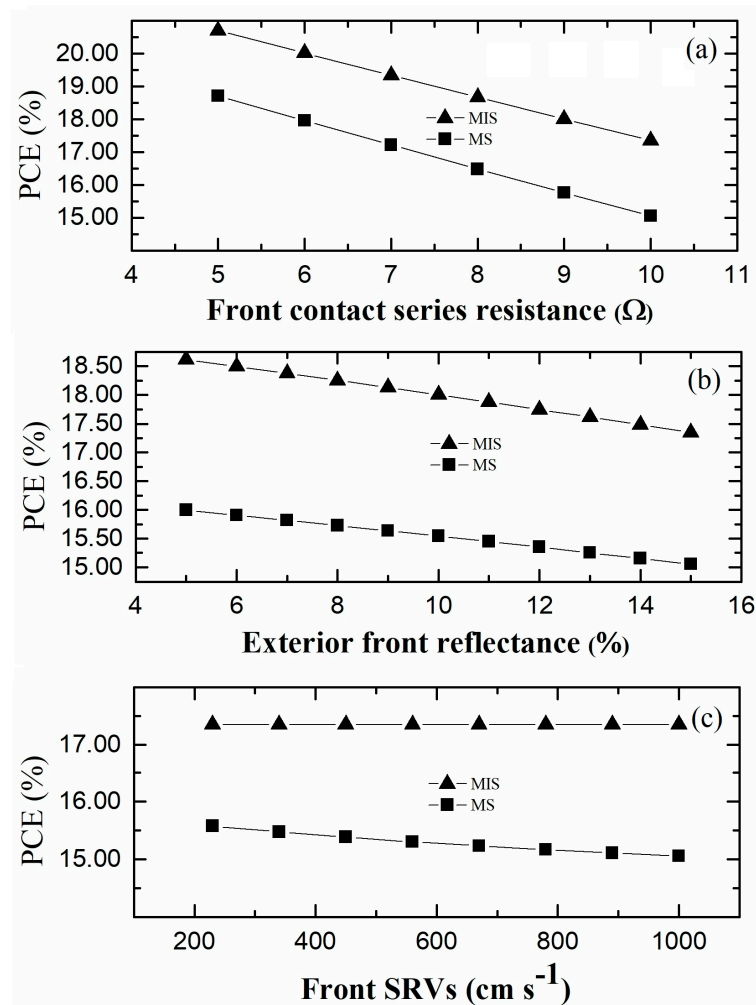


Figure 7. Potential gain in PCE of MS and MIS MXene/n-InP Schottky solar cells due to improved (a) front contact series resistance, (b) exterior front reflectance, and (c) front SRVs.

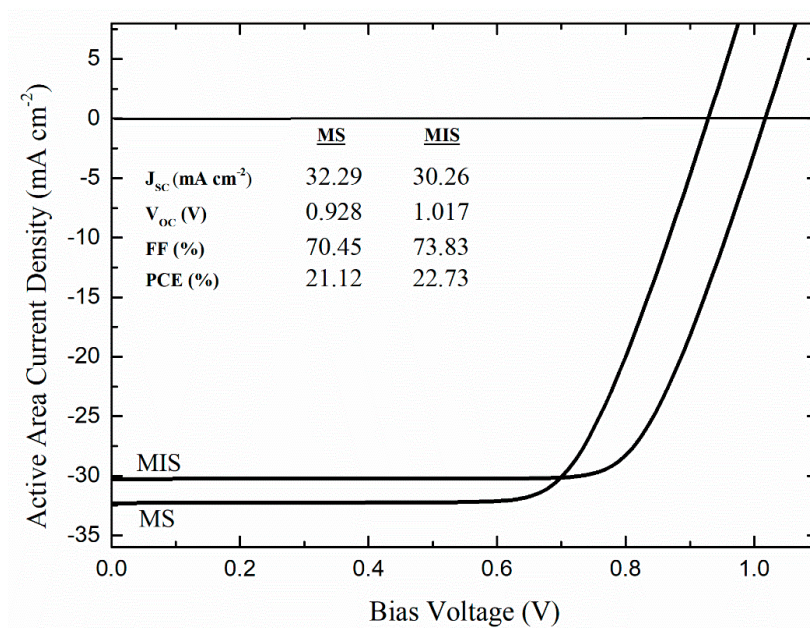


Figure 8. J-V characteristics and performance results for MS and MIS MXene/n-InP Schottky solar cells assuming improved potential gain parameters.

4. Conclusions

A detailed analysis of MXene/n-InP Schottky barrier solar cells designed using PC1D software is presented in this paper. The proposed simple design, in which the functional $\text{Ti}_3\text{C}_2\text{T}_x$ MXene TCE material is deposited using low-temperature solution-processing methods on the thin InP absorber layer can yield high PCEs, possibly over 20%, in both MS and MIS structures, as per the discussed simulation results. These qualities would enable these Schottky barrier solar cells to compete with their InP-based p/n homojunction counterparts in terms of cost-effectiveness. Combining the simpler MS or MIS structures with the anticipated, more affordable InP growth methods [62], such as thin-film vapor-liquid-solid (TF-VLS) growth [63], could lessen the gap and make InP more competitive in the terrestrial market. This is especially true for niche applications that require lightweight and radiation-hard solar photovoltaic cells.

Funding: This research received no external funding.

Data Availability Statement: The original contributions presented in the study are included in the article, further inquiries can be directed to the corresponding author.

Acknowledgments: The researcher would like to thank the Deanship of Scientific Research, Qassim University for funding the publication of this project.

Conflicts of Interest: The author declares no conflicts of interest.

References

1. Ang, T.-Z.; Salem, M.; Kamarol, M.; Das, H.S.; Nazari, M.A.; Prabakaran, N. A comprehensive study of renewable energy sources: Classifications, challenges and suggestions. *Energy Strategy Rev.* **2022**, *43*, 100939. [[CrossRef](#)]
2. Chee, A.K.-W. On current technology for light absorber materials used in highly efficient industrial solar cells. *Renew. Sustain. Energy Rev.* **2023**, *173*, 113027. [[CrossRef](#)]
3. Yamaguchi, M. Radiation-resistant solar cells for space use. *Sol. Energy Mater. Sol. Cells* **2001**, *68*, 31–53. [[CrossRef](#)]
4. Matthew, P.L.; Myles, A.S.; John, F.G.; Robert, J.W. Analytical modeling of III-V solar cells close to the fundamental limit. In Proceedings of the SPIE OPTO Conference, San Francisco, CA, USA, 7 March 2014; p. 898114.
5. Gupta, B.; Shehata, M.M.; Lee, Y.; Black, L.E.; Ma, F.; Hoex, B.; Jagadish, C.; Tan, H.H.; Karuturi, S. Unveiling the Role of H₂ Plasma for Efficient InP Solar Cells. *Sol. RRL* **2023**, *7*, 2200868. [[CrossRef](#)]
6. Ward, J.S.; Remo, T.; Horowitz, K.; Woodhouse, M.; Sopori, B.; VanSant, K.; Basore, P. Techno-economic analysis of three different substrate removal and reuse strategies for III-V solar cells. *Prog. Photovolt. Res. Appl.* **2016**, *24*, 1284–1292. [[CrossRef](#)]
7. Wanlass, M.U.S. Systems and Methods for Advanced Ultra-High-Performance InP Solar Cells. U.S. Patent 9,590,131B2, 7 March 2017.
8. Green, M.A.; Dunlop, E.D.; Yoshita, M.; Kopidakis, N.; Bothe, K.; Siefer, G.; Hao, X. Solar cell efficiency tables (version 62). *Prog. Photovolt. Res. Appl.* **2023**, *31*, 651–663. [[CrossRef](#)]
9. Rühle, S. Tabulated values of the Shockley–Queisser limit for single junction solar cells. *Sol. Energy* **2016**, *130*, 139–147. [[CrossRef](#)]
10. Sree Harsha, K.S.; Bachmann, K.J.; Schmidt, P.H.; Spencer, E.G.; Thiel, F.A. n-indium tin oxide/p-indium phosphide solar cells. *Appl. Phys. Lett.* **1977**, *30*, 645–646. [[CrossRef](#)]
11. Coutts, T.J.; Pearsall, N.M.; Tarricone, L. The influence of input power on the performance of rf sputtered ITO/InP solar cells. *J. Vac. Sci. Technol. B Microelectron. Process. Phenom.* **1984**, *2*, 140–144. [[CrossRef](#)]
12. Li, X.; Wanlass, M.W.; Gessert, T.A.; Emery, K.A.; Coutts, T.J. High-efficiency indium tin oxide/indium phosphide solar cells. *Appl. Phys. Lett.* **1989**, *54*, 2674–2676. [[CrossRef](#)]
13. Rosenwaks, Y.; Li, X.; Coutts, T.J. Characterization of heat-treated ITO/InP solar cells. *J. Vac. Sci. Technol. A* **1997**, *15*, 2354–2358. [[CrossRef](#)]
14. Yoshikawa, A.; Sakai, Y. High efficiency n-CdS/p-InP solar cells prepared by the close-spaced technique. *Solid-State Electron.* **1977**, *20*, 133–137. [[CrossRef](#)]
15. Bettini, M.; Bachmann, K.J.; Buehler, E.; Shay, J.L.; Wagner, S. Preparation of CdS/InP solar cells by chemical vapor deposition of CdS. *J. Appl. Phys.* **1977**, *48*, 1603–1606. [[CrossRef](#)]
16. Purica, M.; Budianu, E.; Rusu, E.; Arabadji, P. Electrical properties of the CdS/InP heterostructures for photovoltaic applications. *Thin Solid Film.* **2006**, *511–512*, 468–472. [[CrossRef](#)]
17. Yin, X.; Battaglia, C.; Lin, Y.; Chen, K.; Hettick, M.; Zheng, M.; Chen, C.-Y.; Kiriya, D.; Javey, A. 19.2% Efficient InP Heterojunction Solar Cell with Electron-Selective TiO₂ Contact. *ACS Photonics* **2014**, *1*, 1245–1250. [[CrossRef](#)]
18. Raj, V.; dos Santos, T.S.; Rougieux, F.; Vora, K.; Lysevych, M.; Fu, L.; Mokkalapati, S.; Tan, H.H.; Jagadish, C. Indium phosphide based solar cell using ultra-thin ZnO as an electron selective layer. *J. Phys. D Appl. Phys.* **2018**, *51*, 395301. [[CrossRef](#)]

19. Raj, V.; Rougieux, F.; Fu, L.; Tan, H.H.; Jagadish, C. Design of Ultrathin InP Solar Cell Using Carrier Selective Contacts. *IEEE J. Photovolt.* **2020**, *10*, 1657–1666. [[CrossRef](#)]
20. Kamimura, K.; Suzuki, T.; Kunioka, A. InP (MIS) Schottky Barrier Solar Cells. *Jpn. J. Appl. Phys.* **1980**, *19*, 203. [[CrossRef](#)]
21. Pande, K.P. Characteristics of MOS solar cells built on (n-type) InP substrates. *IEEE Trans. Electron Devices* **1980**, *27*, 631–634. [[CrossRef](#)]
22. Kamimura, K.; Suzuki, T.; Kunioka, A. Metal-insulator semiconductor Schottky-barrier solar cells fabricated on InP. *Appl. Phys. Lett.* **1981**, *38*, 259–261. [[CrossRef](#)]
23. Li, Y.; Yu, M.; Cheng, Q. Improved performance of graphene/n-GaAs heterojunction solar cells by introducing an electron-blocking/hole-transporting layer. *Mater. Res. Express* **2019**, *6*, 016202. [[CrossRef](#)]
24. Fonash, S.J. *Solar Cell Device Physics*; Elsevier Inc.: Boston, MA, USA, 2010; p. 381.
25. Har-Lavan, R.; Cahen, D. 40 Years of Inversion Layer Solar Cells: From MOS to Conducting Polymer/Inorganic Hybrids. *IEEE J. Photovolt.* **2013**, *3*, 1443–1459. [[CrossRef](#)]
26. Kuphal, E. Low resistance ohmic contacts to n- and p-InP. *Solid-State Electron.* **1981**, *24*, 69–78. [[CrossRef](#)]
27. Alnassar, M.S.N. Discovering new pathways to improved performance of TFSA-doped single-layer graphene/n-Si Schottky barrier solar cells: A detailed numerical study. *Optik* **2024**, *299*, 171640. [[CrossRef](#)]
28. Kong, X.; Zhang, L.; Liu, B.; Gao, H.; Zhang, Y.; Yan, H.; Song, X. Graphene/Si Schottky solar cells: A review of recent advances and prospects. *RSC Adv.* **2019**, *9*, 863–877. [[CrossRef](#)]
29. Yin, X.; Tang, C.S.; Zheng, Y.; Gao, J.; Wu, J.; Zhang, H.; Chhowalla, M.; Chen, W.; Wee, A.T.S. Recent developments in 2D transition metal dichalcogenides: Phase transition and applications of the (quasi-)metallic phases. *Chem. Soc. Rev.* **2021**, *50*, 10087–10115. [[CrossRef](#)]
30. Naguib, M.; Kurtoglu, M.; Presser, V.; Lu, J.; Niu, J.; Heon, M.; Hultman, L.; Gogotsi, Y.; Barsoum, M.W. Two-Dimensional Nanocrystals Produced by Exfoliation of Ti_3AlC_2 . *Adv. Mater.* **2011**, *23*, 4248–4253. [[CrossRef](#)]
31. Guo, Z.; Gao, L.; Xu, Z.; Teo, S.; Zhang, C.; Kamata, Y.; Hayase, S.; Ma, T. High Electrical Conductivity 2D MXene Serves as Additive of Perovskite for Efficient Solar Cells. *Small* **2018**, *14*, 1802738. [[CrossRef](#)]
32. Yu, L.; Bati, A.S.R.; Grace, T.S.L.; Batmunkh, M.; Shapter, J.G. $\text{Ti}_3\text{C}_2\text{Tx}$ (MXene)-Silicon Heterojunction for Efficient Photovoltaic Cells. *Adv. Energy Mater.* **2019**, *9*, 1901063. [[CrossRef](#)]
33. Zhang, Z.; Lin, J.; Sun, P.; Zeng, Q.; Deng, X.; Mo, Y.; Chen, J.; Zheng, Y.; Wang, W.; Li, G. Air-stable MXene/GaAs heterojunction solar cells with a high initial efficiency of 9.69%. *J. Mater. Chem. A* **2021**, *9*, 16160–16168. [[CrossRef](#)]
34. Clugston, D.A.; Basore, P.A. PC1D version 5: 32-bit solar cell modeling on personal computers. In Proceedings of the Conference Record of the Twenty Sixth IEEE Photovoltaic Specialists Conference, Anaheim, CA, USA, 29 September–3 October 1997; pp. 207–210.
35. Kc, D.; Shah, D.K.; Akhtar, M.S.; Park, M.; Kim, C.Y.; Yang, O.B.; Pant, B. Numerical Investigation of Graphene as a Back Surface Field Layer on the Performance of Cadmium Telluride Solar Cell. *Molecules* **2021**, *26*, 3275. [[CrossRef](#)] [[PubMed](#)]
36. Thirunavukkarasu, G.S.; Seyedmahmoudian, M.; Chandran, J.; Stojcevski, A.; Subramanian, M.; Marnadu, R.; Alfaify, S.; Shkir, M. Optimization of Mono-Crystalline Silicon Solar Cell Devices Using PC1D Simulation. *Energies* **2021**, *14*, 4986. [[CrossRef](#)]
37. Parajuli, D.; Kc, D.; Khattri, K.B.; Adhikari, D.R.; Gaib, R.A.; Shah, D.K. Numerical assessment of optoelectrical properties of ZnSe–CdSe solar cell-based with ZnO antireflection coating layer. *Sci. Rep.* **2023**, *13*, 12193. [[CrossRef](#)] [[PubMed](#)]
38. Alnassar, M.S.N. Utilization of open-source software in teaching the physics of P-N diodes. *Comput. Appl. Eng. Educ.* **2023**, *31*, 867–883. [[CrossRef](#)]
39. Jain, R.K.; Flood, D.J. Effects of recombination parameters in p+n indium phosphide solar cells. *Sol. Energy Mater. Sol. Cells* **1997**, *45*, 51–55. [[CrossRef](#)]
40. Piprek, J.; Boer, K.W. InP solar cell improvement by inverse delta-doping. In Proceedings of the First IEEE World Conference on Photovoltaic Energy Conversion—WCPEC (A Joint Conference of PVSC, PVSEC and PSEC), Waikoloa, HI, USA, 5–9 December 1994; pp. 1818–1821.
41. Weinberg, I. InP solar cells for use in space. *Sol. Cells* **1990**, *29*, 225–244. [[CrossRef](#)]
42. Bugajski, M.; Lewandowski, W. Concentration-dependent absorption and photoluminescence of n-type InP. *J. Appl. Phys.* **1985**, *57*, 521–530. [[CrossRef](#)]
43. Sotoodeh, M.; Khalid, A.H.; Rezazadeh, A.A. Empirical low-field mobility model for III–V compounds applicable in device simulation codes. *J. Appl. Phys.* **2000**, *87*, 2890–2900. [[CrossRef](#)]
44. Pearsall, T.P. *Properties, Processing and Applications of Indium Phosphide*; INSPEC/The Institution of Electrical Engineers: London, UK, 2000; p. 300.
45. Vidimari, F.; Pellegrino, S.; Caldironi, M.; Paola, A.D.; Chen, R. High resistivity layers in InP obtained by Co or Fe ion implantation and LPE regrowth. In Proceedings of the Third International Conference Indium Phosphide and Related Materials, Cardiff, UK, 8–11 April 1991; pp. 500–503.
46. Sze, S.M.; Ng, K.K. *The Physics of Semiconductor Devices*; John Wiley & Sons, Inc.: New York, NY, USA, 2007; p. 815.
47. McIntosh, K.R.; Baker-Finch, S.C. OPAL 2: Rapid optical simulation of silicon solar cells. In Proceedings of the Conference 38th IEEE Photovoltaic Specialists Conference, Austin, TX, USA, 3–8 June 2012; pp. 000265–000271.
48. Palik, E.D. *Handbook of Optical Constants of Solids*; Academic Press: San Diego, CA, USA, 1985; p. 804.

49. Aspnes, D.E.; Studna, A.A. Dielectric functions and optical parameters of Si, Ge, GaP, GaAs, GaSb, InP, InAs, and InSb from 1.5 to 6.0 eV. *Phys. Rev. B* **1983**, *27*, 985–1009. [[CrossRef](#)]
50. Schroder, D.K.; Meier, D.L. Solar cell contact resistance—A review. *IEEE Trans. Electron Devices* **1984**, *31*, 637–647. [[CrossRef](#)]
51. Levinshtein, M.; Rumyantsev, S.; Shur, M. *Handbook Series on Semiconductor Parameters*; World Scientific Publishing Co. Pte. Ltd.: Singapore, 1996; p. 232.
52. Khazaei, M.; Arai, M.; Sasaki, T.; Ranjbar, A.; Liang, Y.; Yunoki, S. OH-terminated two-dimensional transition metal carbides and nitrides as ultralow work function materials. *Phys. Rev. B* **2015**, *92*, 075411. [[CrossRef](#)]
53. Jain, R.K.; Flood, D.J. Design modeling of high-efficiency p/sup +/-n indium phosphide solar cells. *IEEE Trans. Electron Devices* **1993**, *40*, 224–227. [[CrossRef](#)]
54. Brandhorst, H.W.; Flood, D.J. The Past, Present and Future of Space Photovoltaics. In Proceedings of the IEEE 4th World Conference on Photovoltaic Energy Conference, Waikoloa, HI, USA, 7–12 May 2006; pp. 1744–1749.
55. Yahia, A.H.; Wanlass, M.W.; Coutts, T.J. Modeling and simulation of InP homojunction solar cells. In Proceedings of the Conference Record of the Twentieth IEEE Photovoltaic Specialists Conference, Las Vegas, NV, USA, 26–30 September 1988; pp. 702–707.
56. Ding, K.; Zhang, X.; Ning, L.; Shao, Z.; Xiao, P.; Ho-Baillie, A.; Zhang, X.; Jie, J. Hue tunable, high color saturation and high-efficiency graphene/silicon heterojunction solar cells with MgF₂/ZnS double anti-reflection layer. *Nano Energy* **2018**, *46*, 257–265. [[CrossRef](#)]
57. Wang, P.; Li, X.; Xu, Z.; Wu, Z.; Zhang, S.; Xu, W.; Zhong, H.; Chen, H.; Li, E.; Luo, J.; et al. Tunable graphene/indium phosphide heterostructure solar cells. *Nano Energy* **2015**, *13*, 509–517. [[CrossRef](#)]
58. Keavney, C.J.; Spitzer, M.B. Indium phosphide solar cells made by ion implantation. *Appl. Phys. Lett.* **1988**, *52*, 1439–1440. [[CrossRef](#)]
59. Goldman, D.A.; Murray, J.; Munday, J.N. Nanophotonic resonators for InP solar cells. *Opt. Express* **2016**, *24*, A925–A934. [[CrossRef](#)] [[PubMed](#)]
60. Aho, T.; Aho, A.; Tukiainen, A.; Polojärvi, V.; Salminen, T.; Raappana, M.; Guina, M. Enhancement of photocurrent in GaInNAs solar cells using Ag/Cu double-layer back reflector. *Appl. Phys. Lett.* **2016**, *109*, 251104. [[CrossRef](#)]
61. McEvoy, A.; Castaner, L.; Markvart, T. *Solar Cells: Materials, Manufacture and Operation*; Elsevier Inc.: London, UK, 2012.
62. Greenaway, A.L.; Boucher, J.W.; Oener, S.Z.; Funch, C.J.; Boettcher, S.W. Low-Cost Approaches to III–V Semiconductor Growth for Photovoltaic Applications. *ACS Energy Lett.* **2017**, *2*, 2270–2282. [[CrossRef](#)]
63. Zheng, M.; Horowitz, K.; Woodhouse, M.; Battaglia, C.; Kapadia, R.; Javey, A. III-Vs at scale: A PV manufacturing cost analysis of the thin film vapor–liquid–solid growth mode. *Prog. Photovolt. Res. Appl.* **2016**, *24*, 871–878. [[CrossRef](#)]

Disclaimer/Publisher’s Note: The statements, opinions and data contained in all publications are solely those of the individual author(s) and contributor(s) and not of MDPI and/or the editor(s). MDPI and/or the editor(s) disclaim responsibility for any injury to people or property resulting from any ideas, methods, instructions or products referred to in the content.